Heliyon 10 (2024) e31963

Contents lists available at ScienceDirect

Heliyon

journal homepage: www.cell.com/heliyon

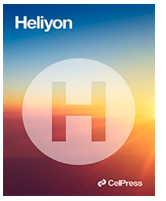

Research article

Hydrochemical characteristics of abandoned coal mines derived acid mine drainage in a typical karst basin (Wuma river basin, Guizhou China)

Lei Yang [a,b], Yuegang Tang [a,*], Hongfu Sun [a], Lingling He [b], Ruiqing Li [a]

[a] School of Geosciences and Surveying Engineering, China University of Mining and Technology, Beijing 100083, China
[b] Guizhou Zhongkuang Environmental Technology Research Institute Co., LTD., Guiyang 55008, China

ARTICLE INFO

Keywords:
Acid mine drainage
Abandoned coal mine
Karst basin
Hydrochemical characteristics
Groundwater

ABSTRACT

The hydrochemical characteristics of acid mine drainage (AMD) were investigated in Wuma River Basin, China. AMD was sampled from nine closed coal mine (CCM) sites to study the temporal and spatial evolution of pH, dissolved oxygen (DO), electrical conductivity (ED), total hardness (THR), total dissolved salt (TDS), and trace elements. The surface water (river) and groundwater surrounding mine sites were sampled to evaluate the potential pollution derived from AMDs. The TDS content of AMD was higher than that of surface water and groundwater. The dominant factors influencing TDS were the pH, temperature, and wet or dry season (which played a role in controlling microbial activity), HCO_3^- balance, and REDOX during the evolutionary process. The hydrochemical type of AMD was dependent on the evolutionary stage. From observations, most AMDs were in the form of the SO_4^{2-}-Ca^{2+}•Mg^{2+} type that was characterized by a low pH, low [HCO_3^-], high [SO_4^{2-}], and high [Fe]. In addition, the AMD samples were undergoing stage **I** and **II** processes, in which SO_4^{2-} and trace elements were generated. The surface water and groundwater were primarily classified as the HCO_3^--Ca^{2+}•Mg^{2+} type, which accounted for their self-cleaning capacity, as indicated by the high [HCO_3^-]. The surface water and groundwater could be affected by the surrounding AMD depending on the geographical location. The surface water and groundwater sites that were located downstream of subsurface and surface runoff were obviously affected by AMD. After being polluted by AMD, surface water and groundwater contained higher levels of trace elements and emerged as the HCO_3^-•SO_4^{2-}-Ca^{2+}•Mg^{2+} type.

1. Introduction

Mining derived acid mine drainage (AMD) is characterized by a high heavy metal content, high [SO_4^{2-}] and low pH (<6.5). AMD generally evolves from sulfide-bearing material that is exposed to oxygen and water in mine waste rock, tailings, and mine pits [1]. Due to its low pH and high heavy metal concentrations, AMD has emerged as a severe hazard to water bodies, soil, and other organisms [2]. Therefore, in recent decades, hydrochemical analyses as well as evaluations of the environmental and ecological effects of AMD have received much attention in China. These physical studies have been accompanied by coal mine structural adjustment policies, resource integration, and initiatives to eliminate excess energy capacity [3]. In the Wuma River Basin (WRB) in Guizhou Province, all 27 pairs of

* Corresponding author.
E-mail address: tyg@vip.com (Y. Tang).

https://doi.org/10.1016/j.heliyon.2024.e31963
Received 17 February 2024; Received in revised form 27 April 2024; Accepted 24 May 2024
Available online 29 May 2024

developed coal mines were ordered to close in 2020. The Wuma River is a first-class tributary of Chishui River, located in Renhuai City. The ecological and environmental protection of the WRB is of great significance to the quality of Chishui River and the entire Guizhou Province because it is listed as a Chinese National Wine special water source, contains the Moutai Scenic Spot, and is also part of a rare fish reserve on the Yangtze River. AMD derived from closed coal mines (CCMs) presents a substantial pollution risk to the whole WRB. It has been widely reported that AMD could induce serious water pollution and damage to aquatic ecosystems in river and groundwater globally [4–8]. Therefore, a comprehensive understanding of the hydrochemistry of AMD derived from CCMs is particularly important for environmental pollution prevention and ecological protection in the WRB.

Preventing coal mines from draining would cause a series of environmental problems, among which changes in the hydrochemical parameters or indicators of rivers are considered the most important. Banks D. et al. recommended categorizing AMD into three types based on chemical characteristics: high salt water, acidic water, and alkaline water [9]. These categories are determined by various factors, including hydraulic conditions, chemical reactions, and biological processes. The hydrochemical properties of AMD were determined to evaluate the environmental impact of mine drainage in the United Kingdom [10]. Lghoul M. et al. studied the hydrochemical characteristics of abandoned mine drainage in the Kettara mine of Morocco [11]. It was found that hydrochemical data were of great importance in the assessment of discharged pollutants and groundwater contamination assessments due to abandoned mine drainage. Moye et al. investigated the evolution of the groundwater environment in the abandoned Kettara mine [12]. The results showed that salinity and the heavy metal content of groundwater surrounding a CCM increased significantly after the mine closure. In a study of water pollution due to abandoned mines in Morocco, Khalil et al. studied 200 abandoned mines using a geographic information system [13]. They found that the acidity of AMD was the most important factor causing water quality pollution.

There are numerous parameters or indicators used to determine AMD hydrochemistry. Charles C. reported that flow rate, water temperature, electrical conductivity (EC), dissolved oxygen (DO), pH, and REDOX potential are the main indexes of AMD (based on 143 coal mines in Pennsylvania, USA) [14]. These indexes affected the morphologies and toxicities of 83 subaqueous substances, including metallic elements and rare elements. The pH value is an important index that impacts on water quality deterioration, mineral oxidation or reduction, and heavy metal leaching. The pH of AMD increases with an increase in flow rate [14]. Compared with a blind coal mine, the AMD flow rate derived from a bituminous coal mine was found to be lower, but the [SO_4^{2-}], [Fe], [Al], [As], [Cd], [Cu], [Ni], and [Sr] were higher [14]. There was a specific correlation between the pH and each component, which was mainly due to three factors: 1) the dilution of surrounding alkaline or neutral water; 2) the solubility of Al, Fe, Mn, Ba, and Sr controlled by a competitive coordination between SO_4^{2-}, hydroxide, and HCO_3^-; 3) SO_4^{2-} complexation and surface complexation reactions. Akburak S. et al. investigated the hydrochemical properties of AMD including pH, EC, water temperature, and DO from 11 open mine pits in Istanbul, Turkey [15]. They found that the AMD had high [K], [Ca], [Na], [Mg], [P], [Fe], [Al], [Mn], [Ni], [Cu], and [Zn]. It was found that the pH of AMD was negatively correlated with P, Ca, Mg, Fe, Al, Cu, Ni, Zn, and Mn; the EC was positively correlated with Ca, Mg, K, and P and negatively correlated with Na; and DO was positively correlated with Fe and Cu, but negatively correlated with water temperature. Tran T. et al. analyzed the hydrochemical characteristics of AMD derived from 28 CCMs in Carboniferous coal-bearing strata (Ruhr region of Germany) [5]. The pH and total dissolved salt (TDS) of the AMD were 6.39–7.35 and 157–1806 mg/L, respectively; the ion concentrations followed the order of $HCO_3^- > Ca^{2+} > SO_4^{2-} > Mg^{2+} > Na^+ > Cl^- > K^+ > NO_3^- > (F^-$ and $Li^+)$; the main hydrochemical types were Ca–Mg–HCO_3–SO_4, Na–Ca–HCO_3–SO_4, Ca–Mg–Na–HCO_3–SO_4, and Na–Ca–Mg–HCO_3–SO_4; and the concentrations of the main ions and TDS increased from south to north [5]. In China, extensive research has been conducted on the hydrochemistry of AMD and its associated water quality, including environmental impact assessments of former mining areas. Xu X. et al. [16] found that the AMD from a mine that was prone to the accumulation and release of natural gases was of the SO_4–Ca–Mg type, which was highly acidic, and had a high salinity and [SO_4^{2-}]. Pan Y. et al. conducted an indoor soil column test to simulate the migration of pollutants (e.g., total hardness, SO_4^{2-}, Cl^-, and total Fe) and pollution mechanism in abandoned mines [17]. Pan Y. et al. conducted hydrogeological and hydrochemical analyses of the AMD from abandoned mines in the Hengshi River area. In addition to a rise in the groundwater level, the hydrogeological conditions were found to have deteriorated and the chemical components of groundwater had changed [18]. The [Ca^{2+}], [Mg^{2+}], and [SO_4^{2-}] increased, while the [Na^+] and [K^+] decreased due to the alternated adsorptions between the cations [19]. Through a hydrochemical simulation, Liu B. et al. inferred that the water environment was weakly alkaline and weakly oxidized in the initial stage of coal mine closure, but then evolved to a weakly reducible environment in the later stage. The weak oxidation conditions were responsible for a gradual increase in the [Fe^{2+}], [Fe^{3+}], and [Mn] in the AMD [20].

Previous studies have revealed that AMD discharged from CCMs has a substantial impact on groundwater and surface water ecosystems. The pollution of ground water and surface water by AMD is mainly controlled by water chemistry. There is a lack of systematic AMD monitoring data for coal-bearing areas in the WRB, preventing the effective prevention of environmental pollution and ecological protection. In particular, groundwater monitoring data for CCM derived AMD in the basin is still lacking. This has prevented a full understanding of the water chemical characteristics and spatial distribution of pollution sources. Therefore, this study aimed to establish an inventory of AMD produced by CCMs in the WRB. The hydrochemical characteristics of coal mine pollution sources and the spatial-temporal changes of the main controlling factors were analyzed. The main controlling factors of the different water quality characteristics were analyzed by combining the geological and mining conditions of CCMs.

2. Overview of the study area

2.1. Natural environment of the basin

The studied CCMs were distributed in the Chishui River Basin, Renhuai City, Guizhou Province, China. Fig. 1 shows the geographical location of the basin, which lies between 106°10'−106°27′ east longitude and 27°27'−27°47'north latitude. In terms of

its geography, the basin consists of undulating mountains with high areas on both sides. The terrain is characterized by the presence of vertical and horizontal gullies, creating a diverse landscape. The area has a subtropical warm and humid monsoon climate, with the dominant wind direction being NW, a high static wind frequency (mean of 39 %), and a mean wind speed of 1.5 m/s. The annual sunshine duration is 1266.7 h, with an annual frost-free period of 270–300 d. The average annual temperature is 18.1 °C, and the maximum is 22.1 °C. Generally, the average annual temperature decreases from the northwest to the southeast. The northwest of Chishui River Basin below 400 m elevation is the hottest part of the region, with an average annual temperature of 17.3 °C–18.3 °C. The distribution of rainfall in the last ten years is given in Fig. 2. The annual average rainfall is 1235.6 mm, with a maximum of 1339.6 mm (2014) and minimum of 881.7 mm (2013). The rainy season begins in early April and ends in October. In the rainy season during this study, the rainfall was 850 mm, which accounted for 80 % of the annual rainfall, and approximately 76 % was concentrated in May to August (up to 600 mm) and could be attributed to heavy rains.

According to the geological structure of Guizhou, the study area was located within the uplifted region of the Tailong platform (I_1), Zunyi's fault arch (I_{1A}), and northeast of Bijie's tectonic deformation area (I^1_{1A}). The geology of the area is mainly characterized by a fold structure, in which faults are mainly distributed in the two wings and core of a fold. The main folds include the central anticline, Changgang syncline, and Maotai syncline. The fold structure is largely characterized by the Luban fault and Sangshuwan fault. The outcrop strata ranges from Cambrian ($\mathcal{C}$) to Quaternary (Q), with Devonian and Carboniferous strata missing. The Cambrian, Permian, Triassic, and Jurassic systems are the most widely distributed and fully developed. The coal-bearing section is the Longtan formation (P_3l), which is dominated by yellow and yellow-brown claystone, sandstone, siliceous rock, and limestone with a thickness of 90–155 m. The overlying Changxing Formation (P_3c) is dominated by a gray-dark-gray thin to thick layer and massive amount of fine limestone with a thickness of 42–72 m. The lower Fumaokou formation (P_2m) is mainly a light gray thick limestone layer, with a thickness of 135–288 m. The geological structure and hydrogeological profile of the study area are shown in Fig. 3. In the west of the study area, the drainage boundary of Longjing, Jiucang, Yuanjiazhai, Flint, Tianbazhai, and Matong is the Jiucang River. The Wuma River serves as the sole drainage area for the whole of the central and eastern regions. Within the study area, the Wuma River flows in an east-west direction, and begins to turn from Wuma Town, eventually merging with the Chishui River in a south-to-north trajectory. The surrounding areas contribute to the water supply of the Wuma River through surface gullies or underground rivers, replenishing and dispersing water on both sides toward the Wuma River. Atmospheric precipitation is the main source of groundwater recharge in the area. There are mutual recharges of reservoirs and ponds in some areas via infiltration and injection through surface cracks, solution

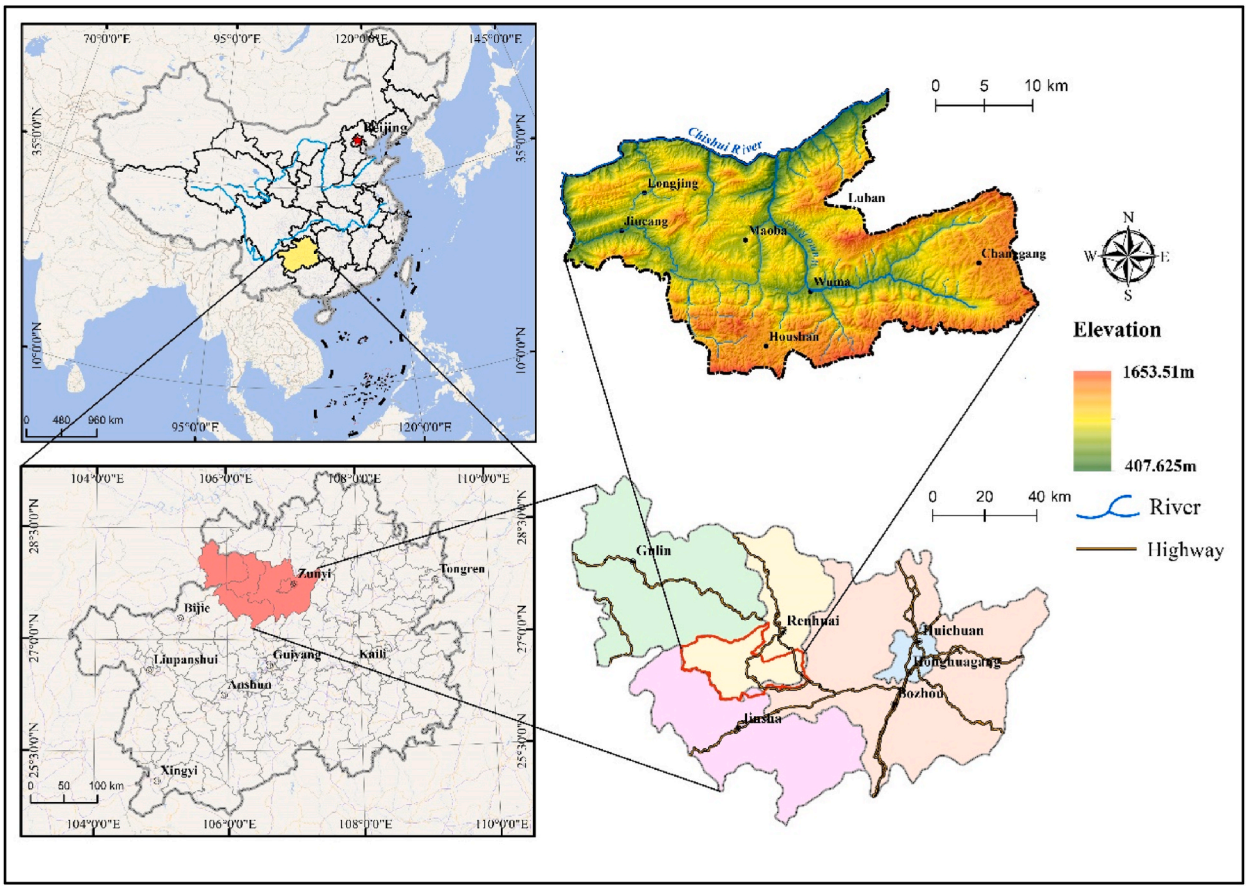

Fig. 1. Administrative division map of the studied Wuma River Basin.

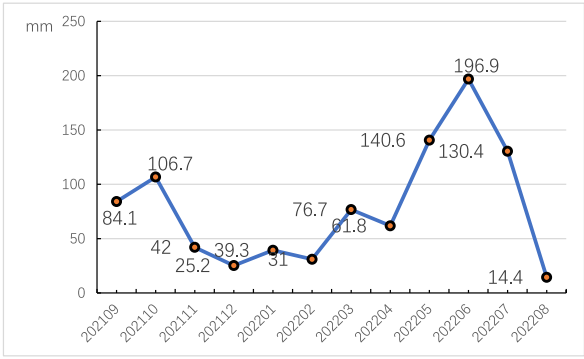

Fig. 2. Monthly precipitation from Sep. 2021 to Aug. 2022 in Renhuai City.

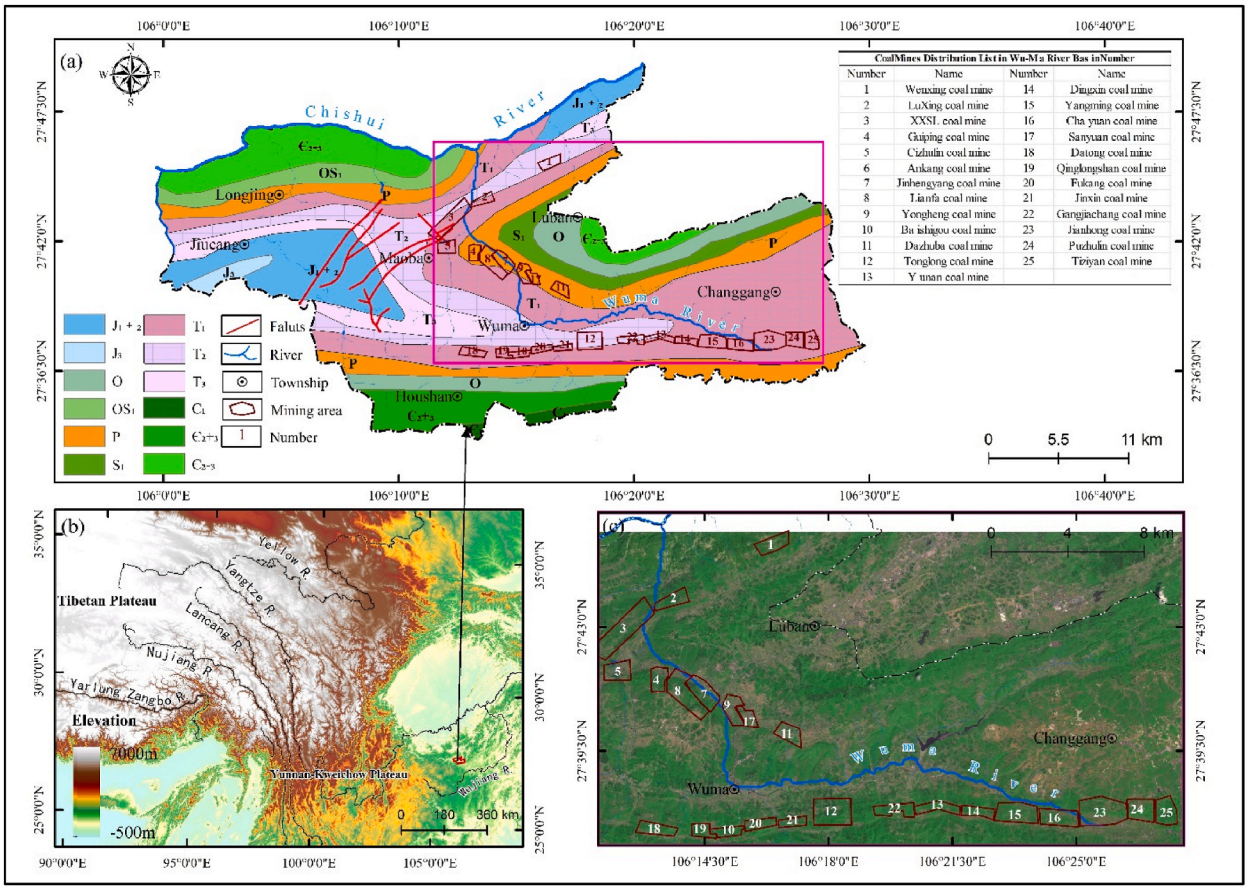

CoalMines Distribution List in Wu-Ma River Bas inNumber

Number	Name	Number	Name
1	Wenxing coal mine	14	Dingxin coal mine
2	LuXing coal mine	15	Yangming coal mine
3	XXSL coal mine	16	Cha yuan coal mine
4	Guiping coal mine	17	Sanyuan coal mine
5	Cizhulin coal mine	18	Datong coal mine
6	Ankang coal mine	19	Qinglongshan coal mine
7	Jinhengyang coal mine	20	Fukang coal mine
8	Tianfa coal mine	21	Jinxin coal mine
9	Yongheng coal mine	22	Gangjiachang coal mine
10	Ba ishigou coal mine	23	Jianhong coal mine
11	Dazhuba coal mine	24	Puzhulin coal mine
12	Tonglong coal mine	25	Tieiyan coal mine
13	Y unan coal mine		

Fig. 3. Distribution map of closed coal mines in Wuma River basin.

gaps, solution troughs, and sinkholes. Due to the strong tectonic action, the developed network cracks, solution gaps, and partial faults are conducive to the recharge process.

2.2. Distribution of CCMs

There are 41 pairs of coal mines in Renhuai City, with 25 of them distributed in the Maotai upstream region of the WRB. All the coal mines in the area are categorized as small mines, with a production capacity of 9–150,000 t/a, and coal is extracted using inclined shafts or the adit development mode. The inclination angle of coal seams ranges from 15° to 55°, most of which have a steep inclination with elevation differences of 300–600 m. Due to the unsophisticated mining methods and limited mining capacity, the formation of

gob (i.e., waste material or leftover coal) only occurs in local areas near the coal seam outcrop. Some coal mines were closed due to technological transformation and were subsequently expanded into medium-sized coal mines, such as the Cizhulin, Ankang, Tonglong, Fukang, Tea Garden, Jianhong, Puzhujing, and Tiziyan mines. Except for Fukang and Tiziyan, most of the remaining coal mines were closed and discontinued before 2012. Fig. 3 shows the distribution of CCMs (in WRB), with the operational aspects provided in Table 1.

3. Methodology

3.1. Sampling

Nine CCMs (labeled as 2#, 5#, 8#, 10#, 11#, 12#, 13#, 15#, and 16#) were selected as research objects (Fig. 4 and Table 1). The groundwater was sampled from springs and a karst cave (total of 20 sites) surrounding these CCMs. The surface water was sampled from nine sections of the WRB and its tributaries, as indicated in Fig. 4. To study the time-dependence of water quality, water from seven of 38 sampling sites was continuously sampled from December 2021 to August 2022. Fig. 4 shows the distribution of sampling sites. The water sample was filtered on-site using a 0.45 μm Whatman® nylon filter, followed by the immediate measurement of pH, DO, temperature, and EC. The filtered water samples were loaded into two polyethylene bottles with volumes of 30 and 250 mL, respectively. The sample bottles were filled completely to replace the air. After collection, the mouth of the bottle was immediately wrapped with sealing film to prevent air entry. The bottles were stored at 4 °C prior to measurements. The cations were measured using the 250 mL bottle water samples. The bottles had previously been cleaned with 6 mol/L nitric acid to guarantee a pH < 2.

3.2. Methods

The anions were measured from the 30 mL water samples without acidification. All samples were measured in the State Key Laboratory of Loess and Quaternary Geology, Institute of Earth Environment, Chinese Academy of Sciences. The measurements included macroions (K^+, Na^+, Ca^{2+}, Mg^{2+}, Cl^-, SO_4^{2-}, NO_3^-, and F^-) and general trace elements (Li, Be, B, Mn, Fe, Co, Al, Cu, Zn, As, Se, Rb, Y, Cd, Ba, Ti, and U). The cations and anions were determined by inductively coupled plasma-optical emission spectroscopy (iCAPTM 7400, Thermo Fisher Scientific, USA) and ion chromatography (Dionex-600, Diones, USA), respectively. The macroions were measured with a precision of 0.01 mg/L within 2 % error. The trace elements were measured by inductively coupled plasma-mass spectrometry (PE NexION 300D, PerkinElmer, USA) with an N9300723 standard sample to guarantee a relative standard deviation (RSD) < 1 %. The [HCO3−] in water samples was determined via charge conservation (H2CO3* ↔ HCO3− + H+, pKa,1 = 6.35; HCO3− ↔ CO32− + H+, pKa,2 = 10.33). In brief, 10 samples were randomly selected and the dissolved inorganic carbon concentration was determined by a Merck alkalinity titration kit (Merck, Germany) with an accuracy of 0.05 mM. The RSD between the dissolved inorganic carbon and [HCO3−] was obtained. An RSD < 5 % was considered to be reliable for the [HCO3−] calculation by charge conservation. The [HCO3−] was calculated using the equations of [21]:

$$HCO_3^- = K^+ + Na^+ + 2 \times Ca^{2+} + 2 \times Mg^{2+} - Cl^- - NO_3^- - 2 \times SO_4^{2-} \quad (1)$$

Table 1
Overview of Basic information for each coal mine in the study area.

Number	Name	Closing time (year)	Coal bed pitch (°)	Mining area ($km^{2)}$	Mining elevation	Drainage method
1#	Wenxing coal mine	2011	37	1.1018	+1040~+600 m	Inclined shaft
2#	LuXing coal mine	2011	49	0.93	+1029 m~+440 m	Adit
3#	XinXingShiLian coal mine	unbuilt	14	3.296	+800 m~+285 m	Adit
4#	Guiping coal mine	2012	20	0.8443	+766 m~+230 m	Inclined shaft
5#	Cizhulin coal mine	2012	17	1.133	+720 m~+250 m	Inclined shaft
6#	Ankang coal mine	2008	21	0.892	+680 m~+150 m	Inclined shaft
7#	Jinhengyang coal mine	2008	16	1.497	+630 m~+250 m	Inclined shaft
8#	Lianfa coal mine	2006	15	2.2265	+620 m~+45 m	Inclined shaft
9#	Yongheng coal mine	2008	18	0.5976	+802 m~+400 m	Inclined shaft
10#	Baishigou coal mine	2005	51	0.557	+1050 m–600 m	Adit
11#	Dazhuba coal mine	2018	32	0.9427	+920 m~+650 m	Adit
12#	Tonglong coal mine	2011	53	2.399	+1200 m~+300 m	Adit
13#	Yunan coal mine	2018	46	0.9344	+900 m~+500 m	Adit
14#	Dingxin coal mine	2018	43	0.7375	+900 m~+580 m	Adit
15#	Yangming coal mine	2008	42	1.875	+950 m~+400 m	Adit
16#	Chayuan coal mine	2012	35	1.4592	+850 m~+400 m	Adit
17#	Sanyuan coal mine	2008	23	0.5976	+780 m~+550 m	Adit
18#	Datong coal mine	2005	44~55	0.993	+900 m~+640 m	Adit
19#	Qinglongshan coal mine	2005	50	0.635	+1000 m~+500 m	Inclined shaft
20#	Fukang coal mine	2019	53	0.714	+1025 m~+330 m	Inclined shaft
21#	Jinxin coal mine	unbuilt	48	0.563	+1015 m~+445 m	Inclined shaft
22#	Gangjiachang coal mine	unbuilt	50	0.9684	+1000 m~+350 m	Adit
23#	Jianhong coal mine	2012	19	2.9	+900 m~+300 m	Inclined shaft
24#	Puzhulin coal mine	2012	18	1.3936	+1000 m~+500 m	Inclined shaft
25#	Tiziyan coal mine	2019	16	1.258	+1266 m~+625 m	Inclined shaft

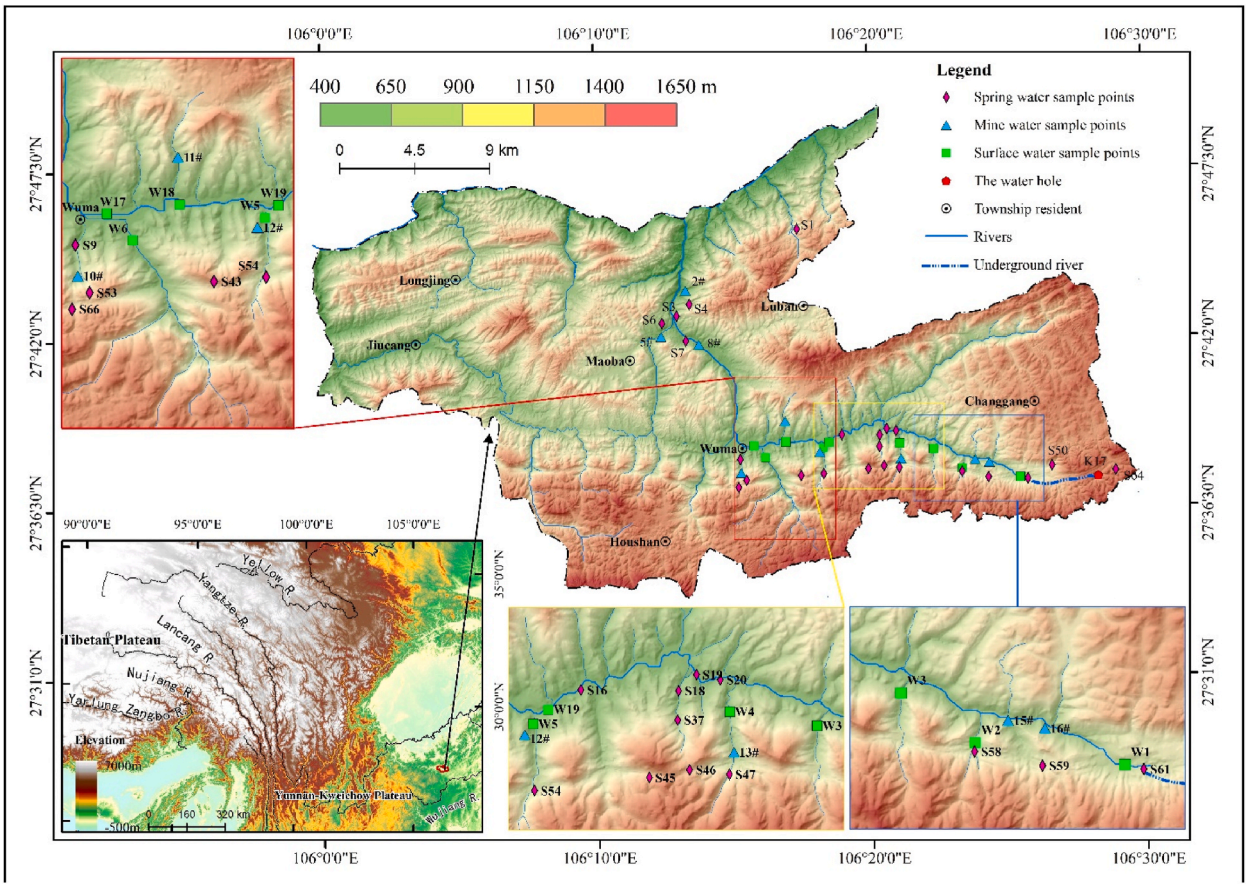

Fig. 4. Sampling sites distribution of surface water, groundwater, and AMDs.

The THR calculated by $CaCO_3$ was expressed as

$$THR = 2.497C_{Ca} + 4.118C_{Mg} \quad (2)$$

where C_{Ca} and C_{Mg} are the [Ca] and [Mg] (mg/L) in actual water samples, respectively. The results from field and laboratory tests for the 38 sample sites are shown in Tables 2 and 3.

Tables 2–1
Hydrochemical index of sampling points in WRB (data reported within ±15 % relative deviation).

TYPE	Parameters	pH	T (°C)	EC (μs/cm)	DO (mg/L)	Hardness (mg/L)	HCO_3^- (mg/L)	F^- (mg/L)	Cl (mg/L)	NO_3^- (mg/L)	SO_4^{2-} (mg/L)
Mine water	Min	2.89	17.10	743.00	1.90	284.55	0.00	0.00	0.63	0.00	277.68
	Max	7.43	27.80	3999.00	5.80	1654.03	298.02	5.30	16.10	36.56	4484.20
	Mean	5.48	21.12	2499.44	4.19	789.07	62.98	1.22	7.23	12.83	1759.75
	SD	1.86	4.20	1587.31	1.13	517.60	125.18	1.64	5.82	12.09	1441.57
	CV	33.96	19.91	63.51	26.89	65.60	198.77	134.62	80.57	94.24	81.92
River	Min	7.93	19.00	373.00	5.30	157.04	25.38	0.05	2.14	6.66	42.75
	Max	8.23	24.30	542.00	7.80	368.77	350.86	6.26	5.46	13.62	375.18
	Mean	8.12	21.58	447.89	6.83	228.01	231.96	0.88	3.72	9.76	110.58
	SD	0.11	2.00	63.17	0.73	68.38	108.22	2.02	1.49	2.73	101.38
	CV	1.31	9.27	14.10	10.65	29.99	46.66	230.47	39.95	27.95	91.68
Groundwater	Min	4.98	16	258	0.8	123.14	0	0	1.38	3.54	21.34
	Max	7.83	20.80	1104.00	6.30	480.89	577.75	0.65	32.58	104.92	459.46
	Mean	7.34	18.19	547.75	4.74	246.51	245.20	0.14	5.54	17.69	112.31
	SD	0.62	1.37	227.77	1.16	104.65	135.22	0.17	6.81	22.54	124.89
	CV	8.44	7.55	41.58	24.48	42.45	55.14	120.97	122.88	127.43	111.20

4. Results and discussion

4.1. Physicochemical parameters of water samples

As shown in Tables 2–1, the pH of water samples was in the range of 2.89–8.23. The mean pH of AMD was lower than that of surface water (river) and groundwater, indicating that mine water (i.e., AMD) was acid, while the surface water (river) and groundwater were weakly alkaline. It is believed that the pH of natural water controls the dissolution, oxidation, and reduction of minerals, especially Fe, Al, and Mn [21]. Fig. 5(a) shows the Kendall correlations between the different hydrochemical indexes for the AMD from 2#, 5#, and 13#, which were sampled from December 2021 to August 2022. The pH was positively correlated with DO and [HCO_3^-], but negatively correlated with trace elements (Fe, Mn, Al, Cu, and Zn). Therefore, trace elements were positively correlated with [H^+], which was favorable for dissolution, but unfavorable for the coordination of trace elements. Negative correlations between pH and trace elements were also found for groundwater (Fig. 5(b)) and surface water (Fig. 5(c)). The mean [Fe], [Al], and [Mn] in Tables 2–2 followed the order of AMD > groundwater > surface water in accordance with the pH, which indicated a deterioration of water quality in the CCMs. The high acidity in AMD led to the dissolution of other metals, such as Ca, Mg Cu, and Zn, which were also present at high concentrations in AMD, as shown in Tables 2–2 At pH < 9, TDS was expressed as

$$TDS = \left[Ca^{2+} + Mg^{2+} + Na^{+} + K^{+}\right] + \left[HCO_3^- + SO_4^{2-} + Cl^-\right] \quad (3)$$

Generally, K^+, Na^+, Mg^{2+}, Ca^{2+}, NO_3^-, HCO_3^-, Cl^-, and SO_4^{2-} constitute 95 %–99 % of the total ions commonly present in natural waters (Tables 2–1 and Tables 2–2). The total concentration of these eight ions in AMDs accounted for 98.54 % of total ions, which was lower than for surface water (99.75 %) and groundwater (99.61 %). The lower proportion of these ions in AMD was attributed to its higher TDS [22]. Fig. 5(a) shows the Kendall correlations for TDS versus [Fe]/[SO_4^{2-}], which were the main characteristic ions indicative of the deterioration of water quality in AMD. The Kendall correlation coefficients of TDS vs [Fe] (>0.6632) and TDS versus [SO_4^{2-}] (>0.8842) were high. The Kendall correlation coefficients were lower for surface water and groundwater, indicating that the water quality of AMD had deteriorated due to acidification. Furthermore, the TDS of AMD (5180.39 mg/L) was more than 11 times that of surface water (439.23 mg/L) and groundwater (463.27 mg/L). The pH was positively correlated with TDS in all waters. The higher TDS in AMD led to a higher THR compared to surface water and groundwater (AMD 789.07 mg/L, surface water 228.01 mg/L, groundwater 246.51 mg/L). As shown in Tables 3–1 and Fig. 7(a), the seasonal/monthly variation of pH in the AMD from 2#, 5#, and 13# were weak, but the pH of AMD from 2# (2.95−3.06) was much lower than that of AMD from 5# (5.89−6.08) and 13# (7.17−7.42). The low pH resulted in higher concentrations of trace elements (Al, Mn, Cu, and Zn) in AMD from 2# than in AMD from 5#, and 13#. The pH was the dominant factor controlling the total ion concentration of AMDs [23].

The average temperature of surface water was similar to that of AMD, but was slightly higher than that of groundwater. The differences in the average temperatures between AMD, surface water, and groundwater were small. However, the EC (mean of 2499.44 μs/cm) of AMD was much higher than that of surface water (mean of 447.89 μs/cm) and groundwater (mean of 227.77 μs/cm). The lowest EC was found at K17 (Fig. 4) and was considered to represent the background value for the study area. The EC is dependent on the total ion concentration and temperature [24]. Fig. 5 also shows that the EC of AMD was positively correlated with most ions, except K^+ and HCO_3^-. Therefore, the high EC of AMD was attributed to the high concentration of ions under similar temperatures (18.19 °C−21.12 °C). Furthermore, Tables 2–1 and Tables 2–2 show that there were different total ion concentrations in the different waters (AMD 5294.48 mg/L, surface water 450.13 mg/L, groundwater 482.83 mg/L). Compared with surface water and groundwater, AMD had a higher metal ion concentration, which resulted in a higher EC and THR (284.55−1654.03 mg/L). The EC of AMD, surface water, and groundwater were negatively correlated with DO, suggesting that most of the DO in the different waters was consumed by microbial activity and oxidation. The lowest THR was observed at S66. However, there was a gradual increase over time (Fig. 2). There were small differences in temperature between the dry and wet seasons. As shown in Tables 3–1, the [HCO_3^-] in the dry

Tables 2–2
Hydrochemical index of sampling points in WRB (data reported within ±15 % relative deviation).

TYPE	Parameters	Na^+ (mg/L)	K^+ (mg/L)	Ca^{2+} (mg/L)	Mg^{2+} (mg/L)	Al (μg/L)	Mn (μg/L)	Cu (μg/L)	Zn (μg/L)	Fe (μg/L)
Mine water	Min	2.44	0.85	79.87	14.97	8.73	12.56	0.67	0.48	39.58
	Max	432.30	40.37	483.30	128.66	89988	27995.32	1374.98	1584.76	248411.29
	Mean	103.23	8.72	199.43	70.69	15018	7209.00	171.97	351.47	49481.19
	SD	146.52	13.15	159.06	48.66	29860.53	8949.84	452.17	525.37	89999.64
	CV(%)	141.94	150.83	79.76	68.83	198.84	124.15	262.93	149.48	181.89
River	Min	1.07	1.23	38.92	9.74	1.12	0.07	0.21	0.32	159.87
	Max	27.10	5.03	100.60	28.55	22.37	10.57	1.35	0.85	466.00
	Mean	8.90	2.45	66.67	14.95	6.18	1.51	0.59	0.50	246.43
	SD	8.43	1.24	21.26	5.58	7.26	3.42	0.35	0.17	91.30
	CV(%)	94.82	50.65	31.89	37.32	117.51	226.34	59.76	33.72	37.05
Groundwater	Min	0.9563	0.4896	30.76	3.04	0.68	0.02	0.11	0.22	398.58
	Max	19.78	36.48	140.90	33.16	3138.60	2345.68	6.04	136.83	3820.456
	Mean	6.15	3.46	78.12	12.49	160.69	193.59	0.80	12.81	1361.23
	SD	5.89	7.83	31.78	7.55	700.94	596.95	1.35	37.87	102736.77
	CV(%)	95.70	226.36	40.68	60.46	436.22	308.35	169.39	295.62	129.45

Tables 3–1
Seasonal dependent hydrochemical index of sampling points in WRB (data reported within ±15 % relative deviation).

Samples	Parameters	pH	T (°C)	EC (μs/cm)	DO (mg/L)	Hardness (mg/L)	HCO_3^- (mg/L)	F^- (mg/L)	Cl^- (mg/L)	NO_3^- (mg/L)	SO_4^{2-} (mg/L)
S1	Dry season	7.66	15.30	1126.50	6.09	581.75	128.82	0.12	10.62	38.95	486.89
	Wet season	6.85	16.88	1019.00	5.48	492.59	83.45	0.16	11.39	46.60	439.83
S45	Dry season	5.48	12.80	1144.50	5.40	459.78	38.90	0.16	21.75	83.41	423.69
	Wet season	5.18	18.30	1044.00	4.06	449.22	3.51	0.20	25.89	96.92	415.36
W1	Dry season	8.42	12.65	506.50	7.77	219.17	233.98	0.06	6.35	11.33	121.91
	Wet season	8.11	19.65	523.50	6.66	236.61	277.10	0.16	4.63	8.61	115.80
W17	Dry season	8.16	12.45	419.00	8.33	215.43	266.96	0.94	5.94	8.56	73.48
	Wet season	7.99	24.73	418.25	6.57	192.12	217.88	0.11	4.36	9.05	77.86
2#	Dry season	3.06	10.65	3999.00	5.43	1149.35	0.00	0.37	6.32	18.01	7446.88
	Wet season	2.95	25.17	3956.67	4.45	2126.40	0.00	4.97	10.97	19.70	4431.90
5#	Dry season	6.08	12.70	3567.00	3.10	750.81	0.00	2.88	56.27	30.53	10391.75
	Wet season	5.89	24.83	2748.25	3.68	893.97	0.00	0.83	15.98	16.05	1704.43
13#	Dry season	7.42	14.10	662.00	5.28	289.36	139.25	0.17	2.73	5.38	238.57
	Wet season	7.17	18.13	1128.50	5.21	347.24	6.55	0.27	3.22	5.93	588.26

Tables 3–2
Seasonal dependent hydrochemical index of sampling points in WRB (data reported within ±15 % relative deviation).

Samples	Parameters	Na^+ (mg/L)	K^+ (mg/L)	Ca^{2+} (mg/L)	Mg^{2+} (mg/L)	Al (μg/L)	Mn (μg/L)	Cu (μg/L)	Zn (μg/L)	Fe (μg/L)
S1	Dry season	13.95	5.23	177.45	33.67	13.73	2105.98	1.24	59.62	724.64
	Wet season	10.02	4.90	151.92	27.50	692.20	2225.57	3.01	103.94	1195.45
S45	Dry season	11.78	26.76	129.30	33.25	2414.54	2007.03	8.54	193.40	534.64
	Wet season	13.60	29.78	128.14	31.39	2467.70	1750.64	5.72	159.65	927.90
W1	Dry season	20.51	1.91	64.50	14.11	2.18	0.05	0.80	0.47	267.73
	Wet season	17.57	2.42	70.75	14.56	2.36	0.43	0.78	0.27	523.70
W17	Dry season	6.61	2.08	64.63	13.13	12.17	56.12	0.58	0.55	271.14
	Wet season	5.73	2.34	58.30	11.30	4.21	1.26	0.44	0.22	467.20
2#	Dry season	34.31	4.44	302.53	95.66	184813.74	48749.50	2527.43	3393.77	1336.50
	Wet season	5.55	3.19	356.25	300.35	100595.78	33943.20	1296.20	2574.32	189.17
5#	Dry season	287.50	33.86	190.83	66.62	2973.65	5417.94	17.67	365.17	435.45
	Wet season	322.57	14.16	246.09	67.87	525.85	3307.90	12.32	141.44	84.35
13#	Dry season	16.36	2.69	80.48	21.47	3.31	578.25	0.60	22.56	320.77
	Wet season	16.68	6.60	103.08	21.82	1923.49	1177.05	12.64	77.43	946.60

season was much higher than in the wet season for groundwater (S1 and S45). This was due to the lower humidity in the dry season, which increased the partial pressure of CO_2 in the atmosphere ([CO2(aq)] = kHpCO2, H2CO3*↔ HCO3− + H+, pKa,1 = 6.35; [HCO3−] = (Ka,1/[H+])kH pCO2):

$$[HCO_3^-] = k_H K_{a,1} 10^{pH} p_{CO_2} \quad (4)$$

where k_H is Henry's constant for CO_2(g). Similar results were found in the AMD from 13#, in which the $[HCO_3^-]$ in the dry season was 21 times higher than in the wet season. The seasonal dependence of $[HCO_3^-]$ in surface water (W1 and W17) was weak. The pH, EC, THR, and DO also displayed weak seasonal dependencies.

4.2. Main cationic and hydrochemical types

Tables 2–2 shows that the SO_4^{2-} and Ca^{2+} were the dominant anions and cations, with concentration ranges of 21−4484 mg/L and 31−483 mg/L, respectively. The average $[SO_4^{2-}]$ and $[Ca^{2+}]$ in AMD were higher than in surface water and groundwater. The maximum concentrations were observed in AMD from 2# and 5#, while the lowest concentrations were observed at S66, which also had the lowest THR. According to the seasonal variations shown in Tables 3–1, the $[SO_4^{2-}]$ and $[Ca^{2+}]$ did not change significantly with seasonal rainfall. The variation of $[HCO_3^-]$ had an observable pH dependency, with a spatial range 0–578 mg/L and a temporal range of 0–971 mg/L. The $[Mg^{2+}]$ had a spatial range of 3–129 mg/L and a temporal range of 0–609 mg/L. It was higher than the $[Na^+]$ in most groundwater samples (except S47, S50, and K17) and surface water samples (except W1). However, a higher $[Na^+]$ than $[Mg^{2+}]$ was found in more than half of the AMD samples (5#, 10#, 12#, 15#, and 16#). For the main ions, i.e., Ca^{2+}, Mg^{2+}, HCO_3^-, and SO_4^{2-}, the differences between AMD/wellsprings and regional groundwater were stronger, with most having significantly higher concentrations in AMD and some wellsprings (S1, S45, and S9). The $[Na^+]$ varied over a wide spatial range (1−432 mg/L) and temporal range (0.2−638 mg/L). The maximum concentration was observed in AMD from #5. Except for S45, the $[Na^+]$ in the other water samples was higher than the $[K^+]$. The maximum $[K^+]$ (40 mg/L) was observed in AMD from 8#. The concentration was <10 mg/L except for at S45, and in the AMD from 5# and/8#. Similarly, the $[Cl^-]$ was <10 mg/L except for at S1/S45 and in the AMD from 2#,/5#, and/8#. The $[F^-]$ was lower than the $[Na^+]$ and $[K^+]$. Except for some CCMs (2#, 5#, 11#) and W3 surface water samples, the $[F^-]$ was <1 mg/

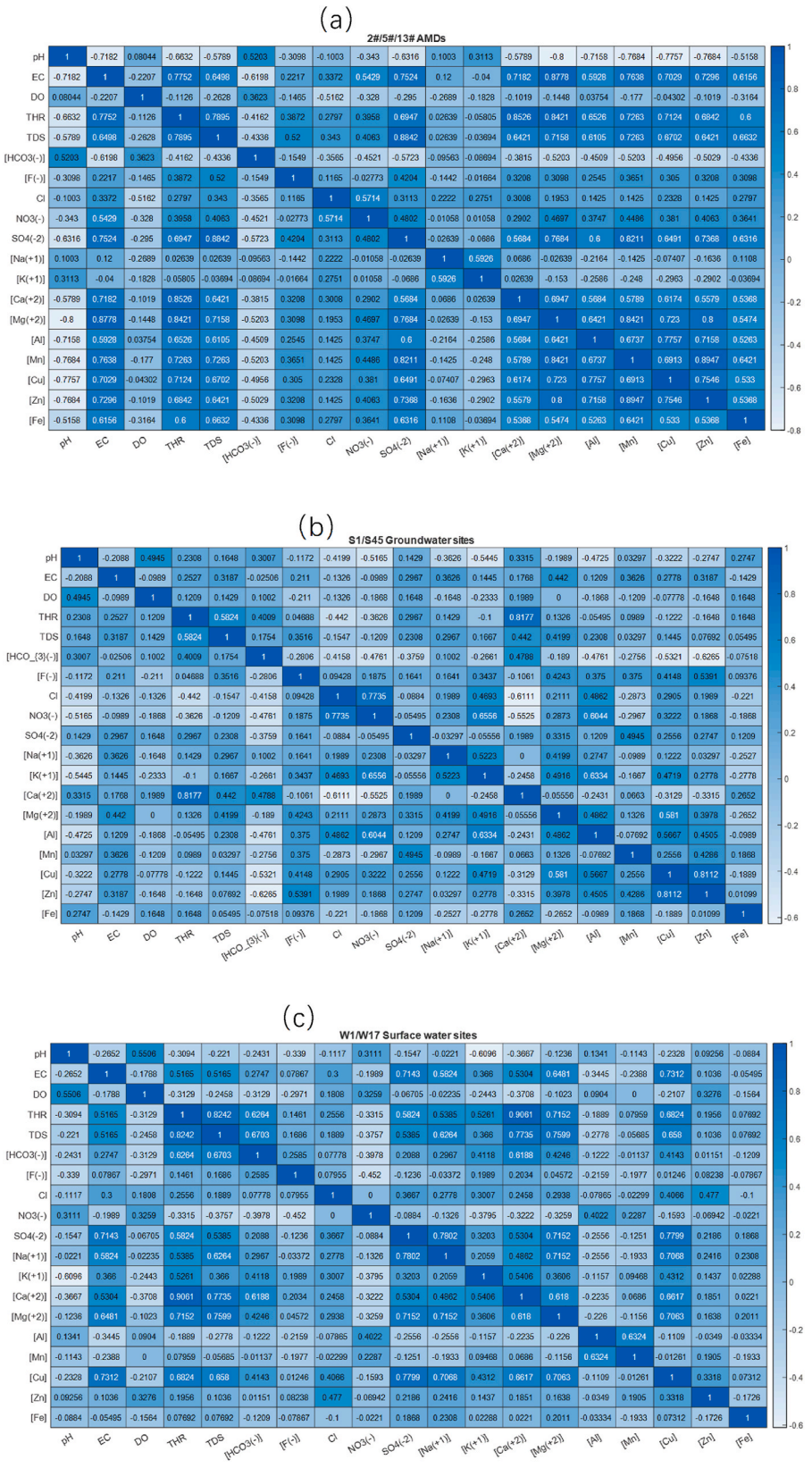

Fig. 5. Kendall correlation analysis between different hydro-chemical indexes.

Fig. 6. Photographs of different AMDs.

L. The ion concentrations are shown in a Piper diagram in Fig. 8, which shows that the surface water and groundwater samples were dominated by the HCO_3^-•SO_4^{2-}-Ca^{2+}, HCO_3^--Ca^{2+}, and SO_4^{2-}-Ca^{2+} hydrochemical types. In contrast, the AMD was characterized by many different hydrochemical types, such as SO_4^{2-}-Ca^{2+}•Mg^{2+}, HCO_3^-• SO_4^{2-}-Ca^{2+}, SO_4^{2-}-Ca^{2+}, SO_4^{2-}-Na^+•Ca^{2+}, and SO_4^{2-}-Na^+•Mg^{2+}. Despite this, the seasonal variations in hydrochemical type were not significant.

4.3. Trace elements

High [Al] and [Mn] in groundwater samples were found at S1, S3, and S45, with maximum values of 3189 μg/L and 2346 μg/L, respectively. The [Al] and [Mn] in the groundwater samples were <10 μg/L and <5 μg/L, respectively. At S1, the concentrations of all trace elements were higher in the wet season than the dry season, as indicated in Tables 3–2 This was attributed to the high temperature and humidities which led to a lower pH ([HCO_3^-]) in the wet season. The low pH and high temperature promoted the oxidation and dissolution of $MnCO_3$/FeS/ZnS/CuS/gibbsite minerals, resulting in high [Mn], [Fe], [Zn^{2+}], [Cu^{2+}], and [Al] [25]. Because S1 was unaffected by AMD (Fig. 4), the wet season which was more preferable for microbial activities improved the oxidation process as indicated by the higher [NO_3^-] than in the dry season. The slightly lower [SO_4^{2-}] in the wet season was attributed to dilution from the increase in runoff volume. For S45, only [Fe] was higher in the wet season despite the lower pH and higher temperature than S1. This indicated that S45 was affected by AMD from 13#. In the surface water, the [Al] of 22 μg/L (W3) and 14 μg/L (W4) were found to be higher than in the groundwater (except S1, S3, and S45). The [Mn] in surface water was <3 μg/L, except at W4, which had a relatively high concentration of 10.57 μg/L. Tables 3–2 shows that the seasonal variation of [Mn] at WI was the inverse of that at W17. The location of W1 was upstream of its nearest CCM (16#) and was considered to not be affected. The higher [Mn] in the wet season was attributed to river wash upstream of W1, which also resulted in a higher [Fe]. In contrast, the [Mn] in the wet season at W17 (1.26 μg/L) was 44 times lower that in the dry season (56.12 μg/L). The location of W17 was downstream of the Wuma River main stream, and was surrounded by 12#, and S54 and W19. The high [NO_3^-] in AMD from 12#, and S54 and W19 was similar to the level at W17, in which the [NO_3^-] was higher than the [SO_4^{2-}] (Fig. 9 (e)). The higher [NO_3^-] meant that microbial activity was more intense, resulting in a higher [Mn] and [Fe] in the dry season [26]. Accounting for the increased water flow in the wet season, the [Mn] of W17 was lower due to downstream dilution, as indicated by the similar [HCO_3^-] to W19 (Fig. 9(e)). In contrast, high concentrations (1010−89,988 μg/L) were detected in the AMD from 2#, 5#, 8#, and 16#. In particular, the [Al] in AMD from 10#, 11#, 12#, 13#, and 15# were much lower (8.7−35.5 μg/L). The [Mn] in AMD was high, ranging from 947 to 27,995 μg/L, except for the low value of 12.6 μg/L found in AMD from 12#. The [Cu^{2+}] in groundwater and surface water were <1 μg/L, except at S1, S45, and W3, which had concentrations of 2.6, 6.0, and 1.35 μg/L, respectively. The [Cu^{2+}] in AMD from 10#, 11#, 12#, 13# and 15# were low (0.67−5.13 μg/L), with values similar to those of groundwater and surface water. However, for AMD from 2#, 5#, 8#, and 16#, the [Cu] was very high, ranging from 16.6 to 1375 μg/L. The spatial distribution of Cu was similar to that of Zn, with concentrations of 109 μg/L at S1 and 137 μg/L at S45, and <2 μg/L in all other groundwater and surface water samples. The [Zn] in AMD from 10#, 11#, 12#, 13#, and 15# (0.48−34 μg/L) were lower than in the AMD from 2#, 5#, 8#, and 16# (359−1585 μg/L). The [Fe] in surface water and groundwater

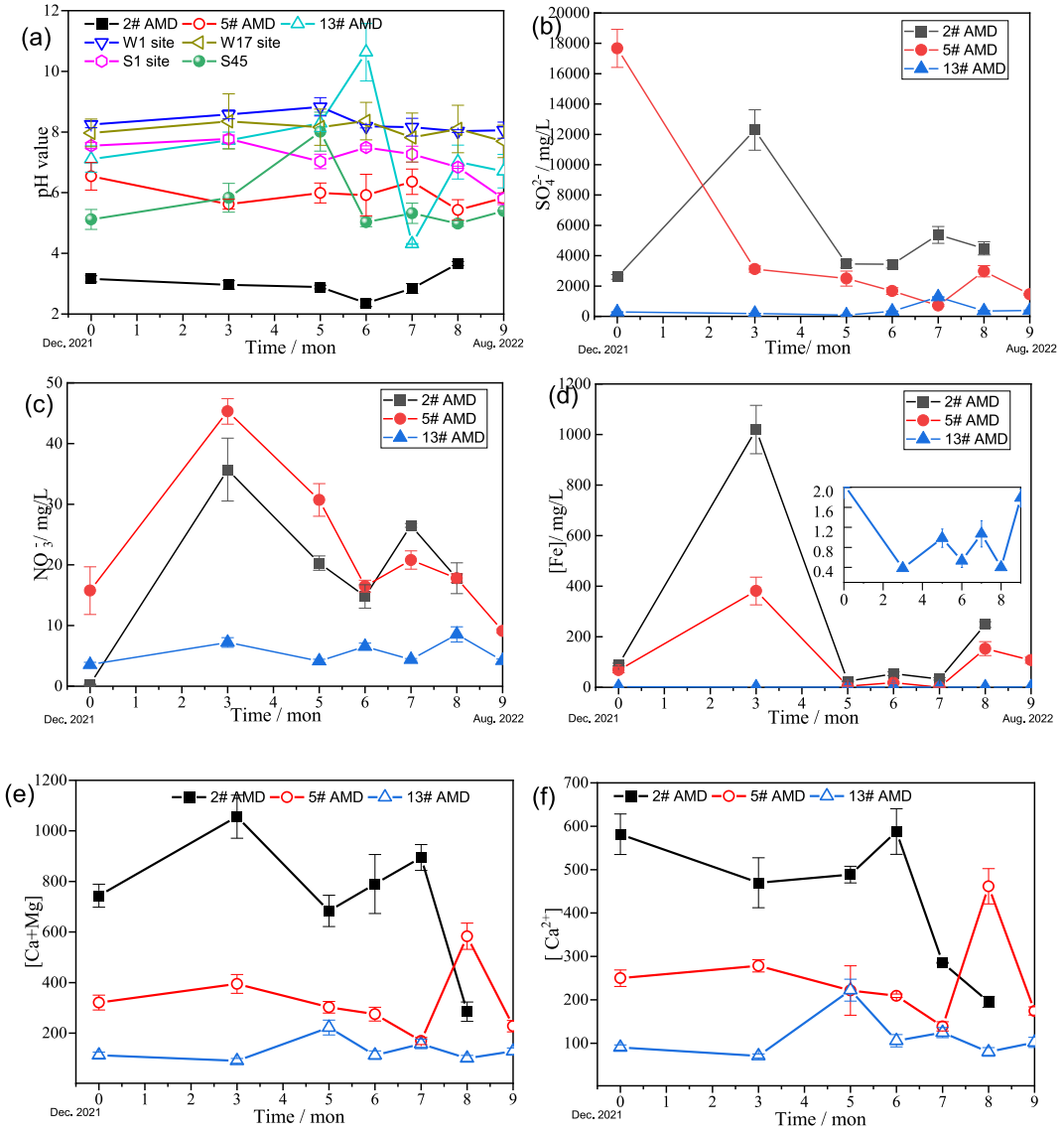

Fig. 7. Monthly variation of indexes in surface water, groundwater, and AMDs.

were <0.6 mg/L. The [Fe] in AMD from 10#, 11#, 12#, and 13# were low (0.4–0.9 mg/L), with values similar to the surface water and groundwater. The concentrations in AMD from 2#, 5#, 8#, 15#, and 16# were high, with a maximum value of 248 mg/L. The higher [Fe] in AMD from 2#, 5#, 8#, 15#, and 16# were proportional to the [Mg^{2+}], [Ca^{2+}], [SO_{42-}], and [NO_3^-] but inversely proportional to [HCO_3^-], as shown in Fig. 9(c) and (f). The low [HCO_3^-] was responsible for the low pH of these AMDs according to Eq. (4). The higher [NO_3^-] enabled greater microbial activity in the AMD from these CCMs. The higher [Fe] as well as the high concentrations of other trace elements were the result of these two factors. Nevertheless, the metal ion concentrations in surface water, groundwater, and AMD generally exhibited no obvious monthly periodic variation at the sample sites. The maximum concentrations at different sampling sites occurred in different months, with the maximum [Al] in August (S1), July (S45), April (W1), December (W17), February [2# and 5#], and June [13#]. The corresponding minimum [Al] occurred in April (S1), August (S45), July (W1), August (W17), December (2#), June (5#), and December (13#). In addition, the maximum and minimum [Mn], [Zn], [Cu], and [Fe] at different sites occurred at slightly different times to those observed for [Al].

4.4. Hydrochemical characteristics of AMDs

4.4.1. Assignments of mine drainage

Mine drainage can be classified into neutral mine drainage (NMD) and AMD according to the International Network for Acid Prevention INAP (2009). The results presented in Section 4.1 suggested that the water in 10#, 11#, 12#, and 13# could be identified

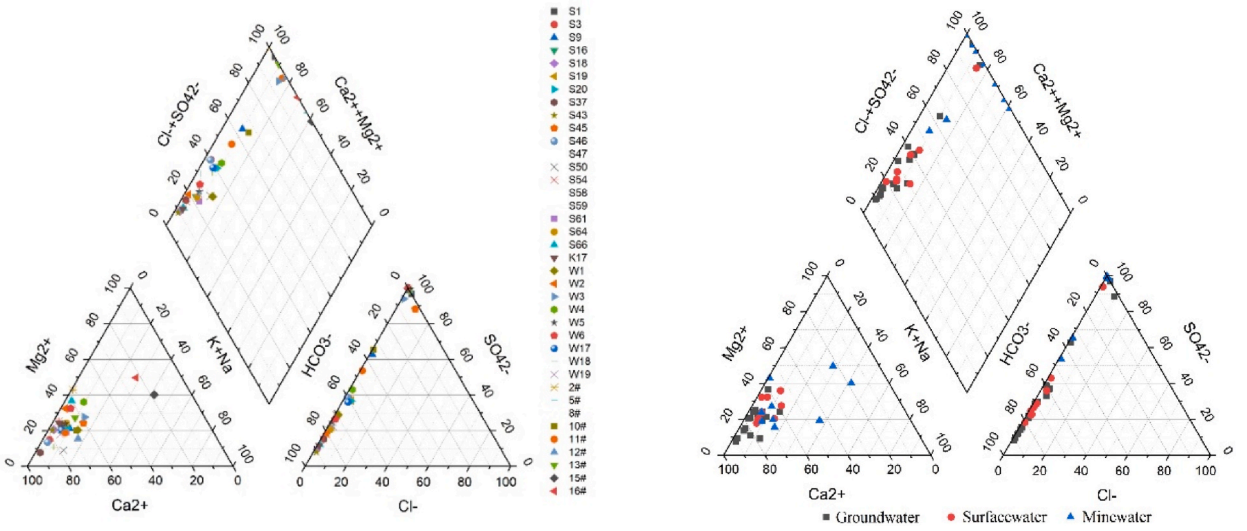

Fig. 8. Piper diagram of different types of water samples in the study area.

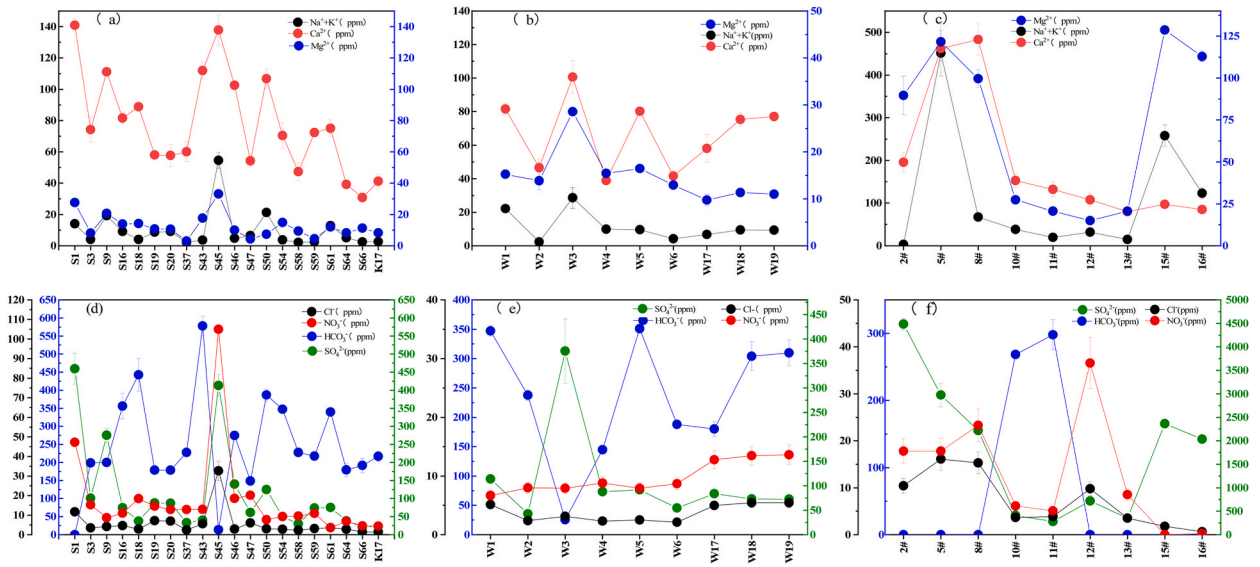

Fig. 9. Spatial distibution of different hydro-chemical indexes in surface water, groundwater, and AMDs.

as NMD with pH > 6 and TDS <1000 mg/L, while the water in 2#, 5#, 8#, 15#, and 16# was recognized as AMD (pH < 6). Furthermore, the EC (> three times), [SO_4^{2-}] (3–10 times), [Mg^{2+}] (3–5 times), and [Fe] (60–500 times) of NMD were much higher than for AMD. The pH had a significant positive correlation with DO (Tables 2 and 3). Compared with AMD, the NMD (10#, 11#, 12#, and 13#) had a lower DO. Jeong H. et al. reported that the lower DO was attributed to FeS oxidation, which relied on atmospheric oxygen rather than DO during the formation of NMD [27]. The cations in NMD and AMD did not change with the pH, suggesting that they were dominated by [Ca + Na] with a concentration >60 %. For the pH-dependent cation concentrations, pH = 2–4, pH = 4–6, and pH > 6 determined the dominant cation types to be Ca, Ca–Mg, and Na, respectively. This pH-dependent transformation of the main cations differed from the results of Tarasenko I. et al. [28]. However, the anions in NMD and AMD were overwhelmingly dominated by SO_4^{2-} and the corresponding EC, [Mg], [Zn], [Mn], and THR were negatively correlated with pH. It has been reported that the pH is not the only criterion that determines the yellow color of mine drainage pollution [29]. The field sampling images in Fig. 6 also show that the mine drainage formed red precipitates in the flow path, indicating that the NMD was a brown-red color, but AMD was a light yellow color.

4.4.2. *Evolution of hydrochemistry in AMDs*

It was considered by Wolkersdorfer C. et al. that the formation of red precipitates in mine drainage occurred in five stages [30].

Stage **I:** reaction initiation: oxidation of FeS by oxygen and water produces a large amount of H^+ and SO_4^{2-}. Stage **II:** heavy metal dissolution. The dissolution of heavy metals (such as ZnS, CuS, and MnS) forms SO_4^{2-} without generating H^+. Stage **III**: oxidation of metal sulfides is accelerated by microorganism under right conditions. Stage **IV**: buffering of the acidity. Carbonate minerals in the surrounding rock (e.g., calcite, dolomite, and siderite) neutralize the H^+ generated in stage **I** and then inhibit the acidification of mine drainage. Stage **V**: mineral precipitates. The oxidization of Fe^{2+} to Fe^{3+} results in the formation of ferrihydrite (FeOOH) precipitates (colloid or mineral). Once the surrounding acceptors (such as soluble carbonate) are deficient, the pH decreases until Fe^{3+} no longer precipitates [31]. As shown in Tables 2–1, the [SO_4^{2-}] had positive correlations with [Fe], [Mn], [Al], [Zn], and [Cu], indicating that the NMD and AMD had undergone stages **I** and **II**. When the process evolved to stages **III** and **IV**, the NMD was appropriate for microorganism growth, and even carbonates in the surrounding rock were consumed. Stages **III** and **IV** resulted in a lower pH, higher [Ca^{2+}], [Mg^{2+}], [SO_4^{2-}], and heavy metals concentrations in NMD. The brown and dark red colors of mine drainage were attributed to the formation of Mn-containing minerals or bauxite. In contrast, the AMD (especially from 10# and 11#) had undergone stage **IV**. The [HCO_3^-] was in the range of 269–298 mg/L, which was attributed to the high proportion of surrounding carbonate, resulting in the corresponding pH increasing to 7.2–7.4. From the concentration ratio between the heavy metals, the AMD from 12# and 13# was slowed down at stage **II**. This was possibly because the surrounding rock could not catalyze the oxidation induced by microorganisms [32]. Fig. 7(a) shows the time (month) dependence of pH for the different waters. For AMD from 2#, the pH had a slight downward trend from December 2021 (pH = 3.16) to June 2022 (pH = 2.36), suggesting it was experiencing stages **I** and **II** with an increasing [H^+], which was subsequently maintained at a high concentration. After June 2022, the pH rebounded to ~3.66. The recovery of the pH of AMD from 2# was attributed to the oxidations occurring in stages **III** and **IV**, in which microbial activity was weak (the [NO_3^-] and [SO_4^{2-}] were lowest at this time). The decline of the [SO_4^{2-}] in AMD from 2# was attributed to precipitation or coordination with other metals. For example, the coordination of SO_4^{2-} with Ca^{2+} generated a $CaSO_4$ precipitate, leading to decline in the [Ca^{2+}], as shown in Fig. 7(f). For AMD from 5#, the pH and [SO_4^{2-}] were maintained at a steady state (Fig. 7(b)), but the [NO_3^-] fluctuated around a higher level than that in the AMD from 2# and 13# (Fig. 7(c)). It was considered that the AMD from 5# was in stage **IV** with a sustained release of Fe (Fig. 7(d)). For the AMD from 13#, the pH was higher (pH = ~7). The [Fe], [NO_3^-], and [SO_4^{2-}] were lower than in the AMD from 2# and 13#. Thus, the AMD from 13# had achieved self-purification and was entering stage **V**.

4.4.3. Spatial variations on hydrochemistry

Tables 2–2 show a strong correlation between TDS and [SO_4^{2-}] and [Fe], indicating that these two indexes were the most suitable for characterizing the surface mine drainage quality. Accordingly, the pollution levels could be evaluated using the average [SO_4^{2-}] and [Fe], which followed the order of downstream (2#, 5#, 8#) > downstream (15#, 16#) > midstream (10#, 11#, 12#, 13#). This indicated that the spatial differences in mine drainage distribution in the WRB were in accordance with the differences in field observations. When the mining conditions and status of CCMs were considered, no correlations were observed between the main ion concentrations and the closing time and drainage mode. In terms of geological conditions, the coal measure strata of the WRB were divided into northern (2#, 5#, 8#, and 11#) and southern (10#, 12#, and 13#) blocks under the influence of the Changgang syncline and Luban fault. In the northern block, 11# was isolated from the downstream coal measure strata due to the Luban fault. The condition of the coal measure strata at 2#, 5#, and 8# were different from the other sites. This difference was reflected by the pyrite content in the surrounding rock of the raw coal. The average [S] of the C7 coal seams in 2#, 5#, and 8# were >2 %. Additionally, approximately 70 % of the total sulfur content in these coal seams was in the form of FeS. The average [S] of the C5 coal seams in 10#, 11#, 12#, and 13# were <1.5 %, while the average [S] of the C3 coal seams in 15# and 16# was 2.25 %. Additionally, the difference in mining scope was directly related to the volume of water accumulation and soluble sulfide content in the goaf (i.e., the void that remains once mining activities are completed) [33]. This was also a critical factor that led to different chemical characteristics of mine drainage. In general, there are large spatial variations in mine drainage [15]. The trends of the main ion (SO_4^{2-}, Ca, Mg, and Fe) concentrations in AMD from 2#, 5#, and 13# were plotted for different periods, as shown in Fig. 9. The variations in the water quality characteristics in these three mines differed from each other.

4.4.4. Temporal variations and geological factors on hydrochemistry

The maximum [SO_4^{2-}], [Ca + Mg], and [Fe] in AMD from 2# occurred in February 2022 (Fig. 7(b)). Their concentrations were significantly higher than the measured values at all other times, which was due to the disturbance to sample sites in August during a severe drought. There were almost no correlations between the temporal variation of rainfall and the concentrations of the main ions in AMD in each of the wet, normal, and dry seasons. This differed from the AMD in Zhijin mining area in Guizhou [34]. In contrast to the temporal trend of rainfall, the main ion concentrations in AMD from 5# displayed a gradually declining trend and then increased after reaching a maximum in December. This indicated that the main ion concentration of mine drainage at this site was reduced due to dilution in May and June. Many plugging treatments were conducted during our sampling period from December 2021 to August 2022. However, the pH in May was >9 and suddenly fell to <5 in June, leading to fluctuations in the main ion concentrations at 5#. Extreme values might be due to the different microbial conditions for forming acid water (i.e., stage **III**), in which microorganisms accelerated the reaction process. After removing the extreme values, the [SO_4^{2-}] and [Ca + Mg] in 2# and 5# exhibited completely opposite trends. Their concentrations were also higher than those of the Fe ion, as shown in Fig. 7.

The extreme values in AMD from 2# occurred in February 2022, and therefore the results for December 2021 were used for the trend analysis. The AMD from 2# was the natural drainage from the abandoned Luxing Coal Mine. Under the new dynamic equilibrium state, the sampling site become a drainage area of the local hydrological unit. Its recharge originated from the Changxing Formation (P3c) overlying coal seam and the underlying aquifer of the Maokou Formation (P2m) whose recharge range changed with the entire karst groundwater head. During the wet season, the runoff time and evaporation intensity of recharge sources are longer and greater

[11], resulting in higher concentrations of Ca and Mg ions being leached out. The longer flow time through pyrite in goaf (i.e., due to reactions with pyrite) increased the [SO_4^{2-}]. In the dry season, the newly-generated $CaSO_4^{2-}$ and Fe_2O_3 deposited on the rock surfaces. This hindered water-rock interactions and lowered the concentrations of the main ions. When AMD from 5# (Guiping Coal Mine) was sampled, all mines were pumping. The water recharge in the goaf was relatively stable. The dissolvation-equilibrium was more easily destroyed after the hydrodynamic conditions were artificially disturbed. However, 5# still maintained temporary underground ventilation during the sampling period. It was able to maintain more balanced oxidation conditions, and therefore had a stronger correlation with atmospheric precipitation.

4.4.5. Key factors effected the hydro-chemical characteristics

Based on this analysis, it was concluded that the main factors controlling the water quality characteristics of mine drainage were: 1) the difference in the [S] and mining scope of raw coal mined before mine closure; 2) the [HCO_3^-] of the surrounding rock; 3) the area and scope of the goaf; 4) the thickness of overlying strata and height of the water-conducting fracture zone in the original coal mine; and 5) the distance between the lowest mined coal and underlying limestone.

4.5. Impacts of mine water pollution on the surrounding water environment

Based on the $Ca + Mg/HCO_3^- + SO_4^{2-}$ ratio (0.7−1), the groundwater was mainly dissolved by carbonate. The TDS of mine drainage was dominated by HCO_3^- and SO_4^{2-} when the ratios were <1 and ~1, respectively. Fig. 9(a) shows the distributions of hardness ions (Mg^{2+} and Ca^{2+}) and Na–K in the sampled groundwaters. At S3, the [Mg^{2+}] and [Na–K] were very low compared with S1, S9, S45, and S50. Tables 3–1 and Fig. 9(d) indicate that the [HCO_3^-] was inversely proportional to the [Mg^{2+}], [Ca^{2+}], and [Na–K], indicating that the water in S3 was much cleaner than in S1. The inversely proportional relationship of [HCO_3^-] to TDS was also found at S43. Because S3 was located upstream of 2# (Fig. 4) with a higher elevation, it was only weakly affected by AMD (2#). The corresponding [HCO_3^-] was mainly controlled by CO_2 dissolution, which led to a relatively higher [Ca^{2+}]. Similar results were found for S43, S50, and S59, which also had a higher [HCO_3^-] but lower [Mg^{2+}] and [Na–K] because they were far from the surface runoff range of the nearest mine (6#). For the observed groundwater sampling sites, S45 had the highest hardness ion (Mg^{2+} and Ca^{2+}) concentrations, as well as [Na–K], [Cl^-], [NO_3^-], and [SO_4^{2-}], indicating that it had the highest TDS, which was inversely proportional to [HCO_3^-] (Fig. 9(a) and (d)). As shown in Fig. 4, S45 was located in the vicinity of 13#, but with a with lower elevation. However, water in S45 had a lower pH than AMD from 13#, and was even lower than the AMD from 5#, as shown in Tables 3–1 The [HCO_3^-] of S45 in the wet season was much lower than that in the dry season, indicating that the groundwater was greatly influenced by terrain and rainfall [35]. To determine the HCO_3^- balance in a closed system ($H_2CO_3^* \leftrightarrow HCO_3^- + H^+$, $pK_{a,1} = 6.35$; $HCO_3^- \leftrightarrow CO_3^{2-} + H^+$, $pK_{a,2} = 10.33$) the proportion of [HCO_3^-] to total organic carbon in the groundwater needs to be determined:

$$\alpha_1 = \frac{[HCO_3^-]}{TOC} = \frac{K_{a,1}10^{-pH}}{10^{-2pH} + K_{a,1}10^{-pH} + K_{a,1}K_{a,2}} \tag{5}$$

According to Eq. (5), the [HCO_3^-] had a maximum value at pH = ~8.3 and was proportional to pH in the pH range of 0–8.3. The low pH at S45 encouraged microbial activity, resulting in enhanced Fe/SO_4^{2-} leaching and FeS oxidation, which occurred more in the wet season than in the dry season (Tables 3–2, 927.90 vs. 534.64 μg/L). The enhanced microbial activity was demonstrated by the higher [NO_3^-] derived from aerobic nitrification (resulting in a lower DO in Tables 3–1). Therefore, the pollution of groundwater was strongly affected by rainfall, which dominated the DO supply of groundwater and led to an increased [Fe] and [SO_4^{2-}] via the microbial oxidation of FeS, as observed at S1 (Fig. 9(a) and (d)). Fig. 9(a) and (d) also showed a higher TDS concentration at S9. Compared with S45, the [SO_4^{2-}] was lower than the [NO_3^-], indicating that the release of [SO_4^{2-}] was mainly responsible for the microbial activity. The pH of water at S9 was higher than at S54 but lower than in AMD from 10# as determined from Eq. (5) and Fig. 9(f). By comparison with S66, which was located in the surface runoff area upstream of 10#, S9 (surface runoff downstream of 10#, Fig. 4) had a significantly higher TDS. Therefore, the pollution of groundwater by AMD originated from the surface runoff downstream [7]. Similarly, at S16 there was a slightly higher TDS than at S43 and S54 (Fig. 4(C)).

Fig. 9 (b) and (e) show that the [Ca^{2+}] and [SO_4^{2-}] at W3 were higher than at W1. The [HCO_3^-] of W3 was much lower than at the other surface water sites (W1, W2, W4, W5, W6, W17, W18, and W19). This indicated that the hydrochemical type of W3 belonged to SO_4^{2-}-Ca^{2+}•Mg^{2+} rather than HCO_3^--Ca^{2+}•Mg^{2+} (W1, W2, W4, W5, W6, W17, W18, and W19). This indicated that W3 was greatly influenced by AMD, and thus water from this area exhibited the hydrochemical properties of AMD. The pH of W3 was lower than that of W1, W2, W4, W5, W6, W17, W18, and W19 as determined from Eq. (5). The release of Ca^{2+} was attributed to dissolution of $CaCO_3$ in the open-system HCO_3^- balance via:

$$CaCO_3(s) \rightleftarrows Ca^{2+} + CO_3^{2-}, K_{sp}^{\ominus} = 10^{-6.32} \tag{6a}$$

$$[CO_3^{2-}] = 10^{2pH} K_{a,1} K_{a,2} k_H p_{CO_2} \tag{6b}$$

$$[Ca^{2+}] = \frac{10^{-2pH}}{K_{a,1}K_{a,2}} \frac{K_{sp}^{\ominus}}{k_H p_{CO_2}} \tag{6c}$$

Equation (6a)−(6c) show that the [Ca^{2+}] was inversely proportional to the pH, indicating that the water at W3 was dominated by $CaCO_3$ dissolution rather than being derived from a decrease in the pH. As shown in Fig. 4, W3 was located downstream of 15# and

16# within the WRB. The higher [SO_4^{2-}], [Ca^{2+}], [Na^++K^+], and [Mg^{2+}] and lower [NO_3^-]/[HCO_3^-] was due to the influence of AMD from 15# and 16#, as shown in Fig. 9(c) and (f) The hydrochemical properties of surface water were closely related to those of AMD. In downstream areas, the surface water was clearly polluted by AMD; but in upstream areas the hydrochemical indexes of W1 (Fig. 4) were the opposite of the AMD from 15# and 16#. Another example of this was W4 (Fig. 4(D)), which was characterized as HCO_3^-•SO_4^{2-}-Ca^{2+}•Mg^{2+} similar to the AMD from 13# (SO_4^{2-}-Ca^{2+}•Mg^{2+}). The slightly higher [HCO_3^-] at W4 could be attributed to the microbial activity at W5. As shown in Fig. 4(C), the samples from W5 in the downstream range of 12# were characterized by the NO_3^--Ca^{2+} type (Fig. 9(c) and (f)). Fig. 9 (b) and (e) showed that some samples from W5 were also characterized by the HCO_3^--Ca^{2+}•Mg^{2+} type, but with the opposite pattern of [HCO_3^-]. This could be explained by the microbial activity, leading to W5 being in stage **II**, in which SO_4^{2-} was formed without the generation of H^+.

5. Conclusions

The hydrochemical characteristics of CCM derived drainage in WRB were investigated. The studied AMDs underwent leaching out of an abundance of Fe, Mn, Zn, Cu, and Al was from the corresponding minerals. Most of the AMDs were found to be the SO_4^{2-}-Ca^{2+}•Mg^{2+} type which was evolving through stages I (reaction initiation) and II (heavy metal dissolution) with prominent DO consumption and H^+/SO_4^{2-} generation. The NO_3^-•SO_4^{2-}-Ca^{2+}•Mg^{2+} type of AMD was dominated by microbial activity that which consumed DO and generated a high [NO_3^-]. The AMD gradually underwent self-purification and was supplemented by rainwater in the wet season, resulting in a higher pH and [HCO_3^-]. The temporal evolution of AMD resulted in changes in the hydrochemical type from SO_4^{2-}–Ca^{2+}•Mg^{2+}→NO_3^-•SO_4^{2-}–Ca^{2+}•Mg^{2+}→NO_3^-•HCO_3^--Ca^{2+}•Mg^{2+}. The evolution of the hydrochemical type of AMD was more significantly affected by precipitation than seasonal temperature variations. As indicated by [Fe], [Mn], [SO_4^{2-}], and [HCO_3^-] indexes, the surface water and groundwater could be affected by the surrounding AMDs. The geographical location and rainfall played the major role in determining the pollution of surface water and groundwater. Pollution by AMD caused the hydrochemical type of surface water and groundwater to change from HCO_3^--Ca^{2+} type to HCO_3^-•SO_4^{2-}-Ca^{2+}•Mg^{2+} and even NO_3^-•SO_4^{2-}-Ca^{2+}•Mg^{2+}.

Data availability statement

The data that support the findings of this STUDY ARE available from the corresponding author, [China University of Mining and Technology-Beijing], upon reasonable request.

Ethics declarations

Informed consent was not required for this study because this study does not involve clinical drugs, animal experiments, race and other ethical issues.

CRediT authorship contribution statement

Lei Yang: Writing – original draft, Visualization, Validation, Data curation. **Yuegang Tang:** Writing – review & editing, Funding acquisition. **Hongfu Sun:** Writing – review & editing, Conceptualization. **Lingling He:** Software, Investigation. **Ruiqing Li:** Software, Data curation.

Declaration of competing interest

The authors declare that they have no known competing financial interests or personal relationships that could have appeared to influence the work reported in this paper.

Acknowledgements

The authors are grateful for the financial support provided by the Project of Guizhou science and Technology Department (No. 20204Y007).

References

[1] A. Akcil, S. Koldas, Acid Mine Drainage (AMD): causes, treatment and case studies, J. Clean. Prod. 14 (2006) 1139–1145.
[2] Y. Jiao, C. Zhang, P. Su, Y. Tang, Z. Huang, T. Ma, A review of acid mine drainage: formation mechanism, treatment technology, typical engineering cases and resource utilization, Process Saf. Environ. Protect. 170 (2023) 1240.
[3] Y. Wu, X. Xiao, Z. Song, Competitiveness analysis of coal industry in China: a diamond model study, Resour. Policy. 52 (2017) 39–53.
[4] G. Thomas, C. Sheridan, P.E. Holm, A critical review of phytoremediation for acid mine drainage-impacted environments, Sci. Total Environ. 811 (2022).
[5] T.Q. Tran, A. Banning, F. Wisotzky, S. Wohnlich, Mine water hydrogeochemistry of abandoned coal mines in the outcropped Carboniferous formations, Ruhr Area, Germany, Environ. Earth Sci. 79 (2020).
[6] P.J.C. Favas, S.K. Sarkar, D. Rakshit, P. Venkatachalam, M.N.V. Prasad, Acid mine drainages from abandoned mines: hydrochemistry, environmental impact, resource recovery, and prevention of pollution, Environ. Mater. Waste Resour. Recover. Pollut. Prev. (2016) 413–462.
[7] J.A. Galhardi, D.M. Bonotto, Hydrogeochemical features of surface water and groundwater contaminated with acid mine drainage (AMD) in coal mining areas: a case study in southern Brazil, Environ. Sci. Pollut. Res. 23 (2016) 18911–18927.

[8] N. Nishimoto, Y. Yamamoto, S. Yamagata, T. Igarashi, S. Tomiyama, Acid mine drainage sources and impact on groundwater at the osarizawa mine, Japan, Minerals 11 (2021).
[9] D. Banks, S.P. Burke, C.G. Gray, Hydrogeochemistry of coal mine drainage and other ferruginous waters in north Derbyshire and south Yorkshire, UK, Q, J. Eng. Geol. 30 (1997) 257–280.
[10] S.B. Banks, D. Banks, Abandoned mines drainage: impact assessment and mitigation of discharges from coal mines in the UK, Eng. Geol. 60 (2001) 31–37.
[11] M. Lghoul, A. Maqsoud, R. Hakkou, A. Kchikach, Hydrogeochemical behavior around the abandoned Kettara mine site, Morocco, J. Geochem. Explor. 144 (2014) 456–467.
[12] J. Moyé, T. Picard-Lesteven, L. Zouhri, K. El Amari, M. Hibti, A. Benkaddour, Groundwater assessment and environmental impact in the abandoned mine of Kettara (Morocco), Environ. Pollut. 231 (2017) 899–907.
[13] A. Khalil, L. Hanich, R. Hakkou, M. Lepage, GIS-based environmental database for assessing the mine pollution: a case study of an abandoned mine site in Morocco, J. Geochem. Explor. 144 (2014) 468–477.
[14] C.A. Charles-Cruz, T.W. Cousens, D.I. Stewart, Compressibility and creep behaviour of hydraulically placed PFA and mine tailings fills, 12th Int. Conf.
[15] S. Akburak, A.A. Kul, E. Makineci, E. Ozdemir, N.K. Aktaş, A.P. Gürbey, H. Yurtseven, M. Köse, T. Akgün, Chemical water parameters of end pit lakes in abandoned coal mines, Arabian J. Geosci. 13 (2020).
[16] X. Xu, Z. Yuan, M. Gong, L. He, R. Wang, J. Wang, Q. Yang, S. Wang, Occupational hazards survey among coal workers using hand-held vibrating tools in a northern China coal mine, Int. J. Ind. Ergon. 62 (2017) 21–26.
[17] Y. Pan, H. Ye, Y. Yang, C. Yang, X. Li, T. Ma, Z. Dang, G. Lu, Transport and fate of Cu and Cd in contaminated paddy soil under acid mine drainage, J. Environ. Manage. 334 (2023).
[18] Y. Pan, H. Ye, X. Li, X. Yi, Z. Wen, H. Wang, G. Lu, Z. Dang, Spatial distribution characteristics of the microbial community and multi-phase distribution of toxic metals in the geochemical gradients caused by acid mine drainage, South China, Sci. Total Environ. 774 (2021).
[19] H. Qiu, H. Gui, L. Cui, Z. Pan, B. Lu, Hydrogeochemical characteristics and water quality assessment of shallow groundwater: a case study from Linhuan coal-mining district in northern Anhui Province, China, Water Sci. Technol. Water Supply 19 (2019) 1572–1578.
[20] B. Liu, S. Ai, W. Zhang, D. Huang, Y. Zhang, Assessment of the bioavailability, bioaccessibility and transfer of heavy metals in the soil-grain-human systems near a mining and smelting area in NW China, Sci. Total Environ. 609 (2017) 822–829.
[21] P.M. Heikkinen, M.L. Räisänen, R.H. Johnson, Geochemical characterisation of seepage and drainage water quality from two sulphide mine tailings impoundments: acid mine drainage versus neutral mine drainage, Mine Water Environ. 28 (2009) 30–49.
[22] A.K. Mohanty, M. Lingaswamy, V.G. Rao, S. Sankaran, Impact of acid mine drainage and hydrogeochemical studies in a part of Rajrappa coal mining area of Ramgarh District, Jharkhand State of India, Groundw. Sustain. Dev. 7 (2018) 164–175.
[23] H. Cheng, Y. Hu, J. Luo, B. Xu, J. Zhao, Geochemical processes controlling fate and transport of arsenic in acid mine drainage (AMD) and natural systems, J. Hazard Mater. 165 (2009) 13–26.
[24] M.C. Jung, Heavy metal contamination of soils and waters in and around the Imcheon Au-Ag mine, Korea, Appl. Geochem. 16 (2001) 1369–1375.
[25] A.B. Sobolewski, A.C. Riese, T.J. Moore, A.R. Brown, Passive treatment of Circumneutral mine drainage from the St. Louis mine tunnel, rico CO: Part 3—horizontal wetlands treatment train pilot study, Mine Water Environ. 41 (2022) 886–905.
[26] N. Ahmed, M. Bodrud-Doza, A.R.M. Towfiqul Islam, S. Hossain, M. Moniruzzaman, N. Deb, M.A.Q. Bhuiyan, Appraising spatial variations of As, Fe, Mn and NO3 contaminations associated health risks of drinking water from Surma basin, Bangladesh, Chemosphere 218 (2019) 726–740.
[27] H.Y. Jeong, Y.S. Han, S.W. Park, K.F. Hayes, Aerobic oxidation of mackinawite (FeS) and its environmental implication for arsenic mobilization, Geochem. Cosmochim. Acta 74 (2010) 3182–3198.
[28] I.A. Tarasenko, A.V. Zinkov, O.V. Chudaev, A.V. Vetoshkina, I.I. Holodilov, Technogenic effect of liquidation of coal mines on earth's entrails: hydrogeochemical aspect, IOP Conf. Ser. Earth Environ. Sci. 87 (2017).
[29] B.S. Acharya, G. Kharel, Acid mine drainage from coal mining in the United States – an overview, J. Hydrol. 588 (2020).
[30] C. Wolkersdorfer, Water management at abandoned flooded underground mines: fundamentals, tracer tests, modelling, Water Treat[M]. Germany: Springer-Verlag Berlin Heidelberg, (2008) 235–377.
[31] J.G. Skousen, P.F. Ziemkiewicz, L.M. McDonald, Acid mine drainage formation, control and treatment: approaches and strategies, Extr. Ind. Soc. 6 (2019) 241–249.
[32] D.K. Nordstrom, D.W. Blowes, C.J. Ptacek, Hydrogeochemistry and microbiology of mine drainage: an update, Appl. Geochem. 57 (2015) 3–16.
[33] L. Dong, X. Tong, X. Li, J. Zhou, S. Wang, B. Liu, Some developments and new insights of environmental problems and deep mining strategy for cleaner production in mines, J. Clean. Prod. 210 (2019) 1562–1578.
[34] X. Li, P. Wu, Z. Han, X. Zha, H. Ye, Y. Qin, Effects of mining activities on evolution of water quality of karst waters in Midwestern Guizhou, China: evidences from hydrochemistry and isotopic composition, Environ. Sci. Pollut. Res. 25 (2018) 1220–1230.
[35] B.C. Maggirwar, B.N. Umrikar, Influence of various factors on the fluctuation of groundwater level in hard rock terrain and its importance in the assessment of groundwater, J. Geol. Min. Res. 3 (2011) 305–317.